Granular media : flow & agitations

Dijksman, J.A.

Chapter 1

Introduction

1.1 Entree

What do sand, rice, coffee powder and Lego® bricks have in common? They are all *granular materials*: collections of non-Brownian, macroscopic particles with dissipative interactions. Despite their obvious relevance and their overabundance in nature, industry and households, the macroscopic mechanical properties of these materials are not well understood. The main theme of this thesis will be an experimental study of the properties of precisely these granular materials under weak driving. Due to their dissipative nature, energy has to be supplied, for example by shaking or shearing, in order to observe dynamics.

Chapters 2-5 deal with the flow of granular media in so-called *split-bottom* geometries, which in essence consist of a disk rotating at the bottom of a container. We study dry granular flows, both in the frictional, slow, rate-independent regime, and the liquid-like, rate dependent regime which is reached for faster flows. We shall also study suspension flows. We develop the so-called index matched scanning technique, that allows 3D imaging of the suspensions. Also for the suspension we study both the slow, rate independent and the faster, rate dependent regime. In all cases we combine 2D and 3D imaging of the flow with rheological measurements. Previously, the rheology of the split-bottom experiments had not been studied experimentally. We discuss here how to deal with the steep gradients arising near the split, and focus on the functional dependence of the driving torque as a function of flow rate and filling height. Both for the filling height and for the flow rate dependence, we

discuss and test recent theoretical predictions.

In chapter 6 and 7, the granular medium is also agitated by vibrations. Chapter 6 deals with slow granular flows in the split-bottom geometry, when this system is subjected to weak vibrations. Fluctuations play a crucial role for granular flows, and the additional vibrations allow us to tune the amount of fluctuations independently from the flow rate. These strongly affect the phenomenology -- even very weak vibrations completely destroy the rate-independent nature of slow granular flows, which are a hallmark of non-vibrated grain flows. In chapter 7 we revisit the classical tapping induced compaction experiments. By carefully controlling both the strength and duration of the taps, we find that not the peak acceleration, but rather the time of flight of the grains controls their behavior.

This chapter -- In section 1.2 we will consider what makes granular media interesting and sets them apart from other many-body systems in Nature. In section 1.3, we will give an overview of what is known of the basic phenomenology of slow granular flows. In this thesis we will study slow granular flows in a particular flow geometry called the *split-bottom* geometry; in section 1.4 we will therefore give a detailed overview of the current knowledge of granular flows in these systems. In section 1.5 we briefly review various theoretical approaches to granular flows, in particular the so-called *inertial number* theory. Although mostly applied to fast granular flows, it has also yielded insight in the nature of slow flows.

1.2 Granular Media

Macroscopically, granular media exhibit a complex mixture of solid and fluid-like behavior. This is commonly illustrated by the fact that it is possible to walk on completely dry beach sand, which supports one's weight as if it were a solid. By scooping up a handful of this sand, and letting it run through one's fingers, the fluid-like nature of the material is also immediately obvious.

Microscopically, this complex behavior has various sources. First of all, the mere size of the granular constituents makes them insensitive to thermodynamic temperature: the gravitational energy mgd of a 1 mm sand grain exceeds k_BT by 14 orders of magnitude. This implies that a thermal equilibrium as understood in the statistical mechanics framework is never reached. Interactions between the grains are dissipative -- kinetic energy of a macroscopic particle can always be transformed into thermal energy of the atoms and molecules that make up the particle. For example: a glass marble dropped on a glass plate rebounces to ever

smaller heights. The athermal and dissipative nature of the microscopics leads to systems very far from equilibrium. In particular, when not externally driven, granulates condense into a (meta)stable, quiescent state: a bag of glass particles dropped on a glass plate comes to rest virtually instantaneously. Interactions between particles are usually only weakly attractive, if at all. This makes granular materials easily deformable on macroscopic length scales, if no external pressure is applied. The interaction potentials between individual particles are at the same time also highly nonlinear, and involve many length and timescales [1].

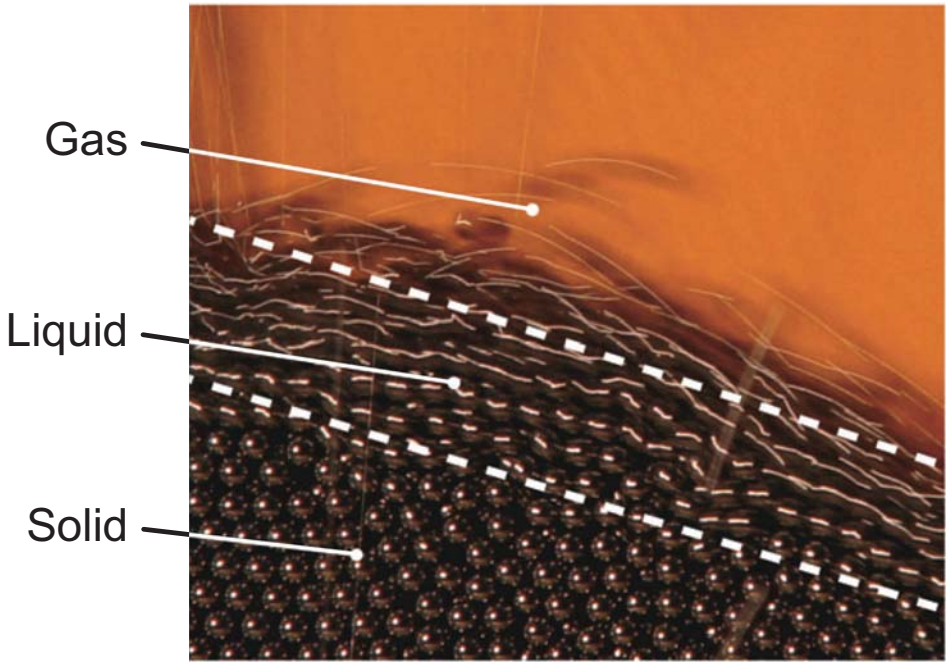

Figure 1.1: A motion-blurred image of steel beads poured on a pile illustrates the three distinct phases of granular material. Figure adapted from Ref. [2]. Reproduced with permission. Copyright (2008) Annual Review Inc.

Granular solids, liquids and gases -- A common trisection of granular materials is to view them as being either solid, liquid or gas-like, depending on the way the material is driven [2, 3]. An illustration of this viewpoint is shown in Fig. 1.1. Steel beads are poured on a heap from which they flow down, and exhibit the three phases: on top of the flow down the heap, there is a dilute phase where collisions are the dominant interaction between the beads. This

thesis will not touch upon this regime; we refer the reader interested in this *gaseous* regime to review articles like Ref. [4]. In the semi-dilute phase just below this granular gas regime, beads also have enduring frictional contacts, but still flow easily past each other. With increasing distance to the surface of the heap, this *liquid* phase then crosses over into a phase in which the particles do not have much free volume anymore to move past each other, and do not experience collisions anymore, but only have enduring contacts. This phase is referred to as the *solid* phase; in this phase the particles are essentially static.
This complex behavior of granular materials is often hard to predict or capture in models. At present, there is for example no *general* approach which, for given flow geometry, driving strength and grain properties, predicts the ensuing granular flow fields. Given the ubiquity of granular materials, it is evident that such modeling is highly desirable. Apart from being studied for the utilitarian value of a better understanding of them, granular materials also serve as a model system to study the *jamming* transition. This phase transition, separating a disordered solid- and liquid-like phase is speculated to be exhibited not just by granular materials, but by many different kinds of disordered systems, such as colloidal suspensions, emulsions and foams. The jamming concept therefore has the potential of underpinning a universal framework for the description of such disordered systems. The study of granular materials has contributed greatly to the development of this theory, although many questions remain unanswered.

In this thesis we will focus on the boundary between the liquid and solid phase by studying slow granular flows. What do we mean by slow? As will be detailed in Section 1.5.1, we can compare the shear rate $\dot{\gamma}$ in the granular flow to the rearrangement timescale of a particle inside this flow. The simplest timescale one can construct with the relevant variables ρ (the density of the grains), P (the local pressure acting on the particle), and d (its diameter) is the time it takes for a particle to move over a distance d given that it is exposed to a pressure difference P: $d/\sqrt{P/\rho}$. For $\dot{\gamma}$ small compared to $d/\sqrt{P/\rho}$, so for $\dot{\gamma}d/\sqrt{P/\rho}$, we call the flow *slow*. In this regime, particles interact via enduring contacts, and inertial effects are negligible.

Two features of slow flows are very robust. Whatever the driving geometry, the average forcing required to sustain a certain flow rate becomes independent of the driving rate. Likewise, the obtained flow profiles become independent of the driving rate. Therefore, we refer to the regime of slow flows as the *rate-independent* regime. In the literature the term *quasi-static* is also very often used to refer to this regime. This rate independence is due to the fact that

the dominant type of interaction between the particles is frictional, and sliding friction is at most only weakly dependent on the sliding velocity [5].

1.3 Slow Flow Geometries: Planar, Couette and Chute

To study granular flows, one has to induce motion in the grains. This can be done by imposing a force or, equivalently, a *stress* -- a force per unit area -- on the material, or a deformation or *strain* -- a deformation per unit length.
In a typical flow geometry called the *inclined plane*, a constant stress is applied. A table is placed at some angle with respect to gravity, and grains are poured onto this table from a large reservoir -- see Fig. 1.2a. The constant stress, acting on the grains, depends on the tilt angle of the table. The special character of the behavior of granular material is however such that in decreasing this stress smoothly to zero, by reducing the tilt angle of the inclined plane, its resulting flow speed will not go smoothly to zero -- below a certain threshold inclination, the flow will come to a halt; the packing *jams*.

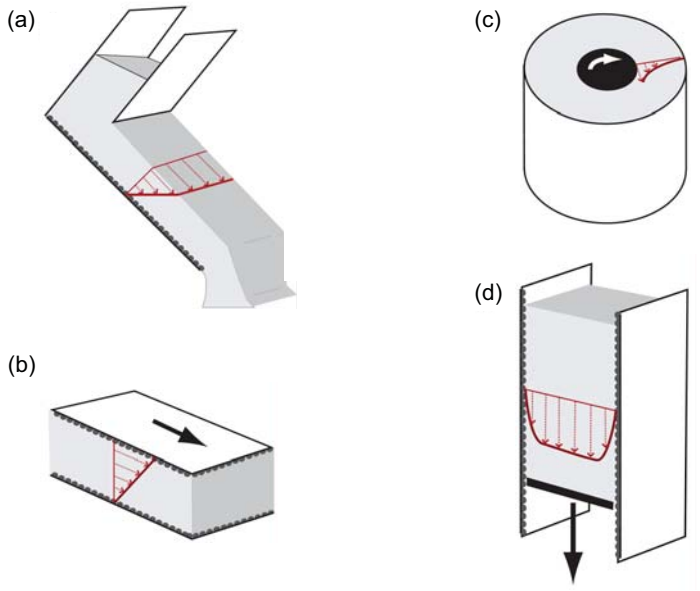

Figure 1.2: Four different flow geometries. (a) inclined plane; (b) plane shear; (c) Couette ; (d) chute. Figure adapted from Ref. [2]. Reproduced with permission. Copyright (2008) Annual Review Inc.

To study arbitrarily slow flows, one therefore has to *impose* deformation,

since this can then be done at arbitrary rate. The canonical way to do this is to use some container with a constantly moving, rough boundary. This is usually accomplished in one of the three following different geometries: planar, in which granular material is sheared between two parallel plates (Fig. 1.2b); Couette, where shear takes place between an inner and an outer cylinder (Fig. 1.2c), and the chute flow geometry (Fig. 1.2d), which is essentially a rectangular, vertical pipe. Chute flow does not involve a physically moving boundary; shear is driven by gravity as in the inclined plane geometry. In contrast to the inclined plane flow, the flow rate in the silo, and with that the shear rate, can be made extremely small by adjusting the flux of particles at the bottom.

Note that if one drives the system externally, for example by means of vibrations, a constant force is usually also sufficient to set up an arbitrarily small but constant flow speed [6, 7], irrespective of the geometry. We will also apply this principle in the split-bottom geometry to induce constant flow under constant applied stress -- see chapter 6.

Another common rheometric geometry is notably absent in the literature on the flow properties of granular materials: the cone-plate geometry [8]. In this geometry, material is sheared between a rotating cone and a static plate. The advantage of cone-plate geometries is the fact that the shear stress in the gap is constant [8]. The only setup that setup that comes close to the cone-plate geometry is the wide plate-plate setup used by Lu [9, 10]. The reason why cone-plate geometries are not used is simple: confining material in the cone-plate gap is normally achieved by the surface tension of the fluid. Granular materials do not have surface tension, since they do not have attractive interaction potentials. Therefore, one would have to confine the granular materials inside the gap with side walls positioned very close to the edge of the disk (as in the plate-plate geometry from Refs. [9, 10]), which creates nonuniform shear conditions at the outer edge of the cone.

In this section, we shall describe the basic phenomenology of slow granular flows observed in the plane shear, Couette and chute geometries. For all geometries, we will describe the main experimental parameters and discuss experimental and numerical observations of the velocity profiles, stresses and dilatancy effects, if available.

Apart from the setups described above, there is another geometry that allows one to impose deformations at a constant rate: the split-bottom geometry. In the split-bottom geometry, the source of the driving is a buried, rotating disk. Since the split-bottom geometry is the geometry we shall use in almost all experiments covered by this thesis, the flow behavior observed in this flow cell warrants a more detailed description, which will be given in section 1.4.

1.3.1 Plane Shear Flow

The simplest way to impose shear deformation is in a plane shear geometry, depicted in Fig. 1.2b. In this geometry, there are two control parameters: the shear velocity V and the gap size W. Numerical work has shown that for slowly driven systems, these velocity profiles at short times are highly intermittent [11], and that, averaged over enough strain, a linear profile is always recovered, also in the rate independent limit [12]. Note that in experiments linear profiles are seldom observed [13].

Dilatancy has been observed already very early in plane shear experiments [14]. Kabla [15] confirmed quantitatively that dilatancy in slow granular flows is a function of the total strain in the sample. These X-ray experiments revealed the following relationship between the strain s and volume fraction Φ:

$$\Phi(s) = \Phi_{min} + (\Phi_{max} - \Phi_{min}) \exp(-s/s_c), \tag{1.1}$$

where s_c is a characteristic amount of strain after which equilibrium is reached.

Of all the geometries mentioned, plane shear is easiest to realize in numerics, but very hard to study experimentally. To obtain a constant stress, gravity has to be eliminated, and for steady state flow analysis, large strains are necessary, which are difficult to obtain in experiments. To circumvent these problems, Couette and chute experiments are usually carried out.

1.3.2 Couette Flow

Apart from grain properties, the system parameters for the Couette geometry are the radius of the inner wheel R_i and the outer wheel R_o, the dimensionality (two or three), and driving rate Ω. The flow localizes near the moving boundary in a *shear band*. This shear banding is generally very strong, with bands having a typical thickness of five to ten grain diameters. Shear banding appears to be robust: studies in Couette cells always show the formation of a narrow shear band near the inner cylinder, irrespective of dimensionality and driving rate [16]. Close to the driving wall, the velocity profile in Couette flows can be expressed as the product of an exponential and a Gaussian [16, 17]:

$$v_\theta(r) = v_o \exp[-b(r/d)] \exp\{-[c(r - r_o)/d]\}^2, \tag{1.2}$$

Here $v_\theta(r)$ is the velocity profile, v_o, b and c and r_o are fitting constants that depend on the particle shape and roughness. d is the particle diameter. This velocity profile was also found in rate independent flows in an annular shear cell [18]. Further away from the wall, purely exponential tails were observed [19].

Note that for small gaps, where $R_i - R_o$ is of the order of a few particle diameters, a linear profile is observed [20].

The average driving stresses necessary to sustain a constant rotation rate in these Couette flows are generally independent of Ω. Hartley [5] found a weak logarithmic dependence on Ω for slightly compressed systems. The stresses can show large fluctuations though, since the flow can be intermittent [5]. In the intermittent flows, Eq. 1.2 is only obtained after time averaging. In two dimensions, below a certain critical volume fraction of about 0.78, the stress necessary to drive the flow disappears completely; above this volume fraction, the logarithmic rate dependence increases with the distance to this critical filling fraction [5]. These large filling fractions were obtained with relatively soft particles, with a Young's modulus of 4.8 MPa [17]. Rigid grains like glass beads, which have a Young's modulus of the order of GPa, are only slightly deformed in a typical experiment, so they are typically close to this critical fraction [21], which means that their logarithmic dependence is probably weak.

Shearing frictional granular materials induces *dilatancy*, an increase in volume of a fixed amount of grains. This was already observed by Reynolds [22]. He filled a bag with shot and water to its maximum capacity, and noticed he could add extra water after deforming the bag, showing an increase in the interstitial volume due to the deformation. Dilatancy is also observed in Couette geometries. Closer to the driving wall, the dilatancy is more pronounced [16, 23, 24].

1.3.3 Chute Flow

In chute flow, also sometimes called *silo* flow, the main control parameters are the width of the channel W and the flow rate imposed at the outlet Q [25]. The flow profile is that of plug flow, with narrow shearbands at the edges [26]. A typical plug flow profile is indicated in Fig. 1.2b. This flow profile is found for essentially all flow rates [27], including the rate independent regime. Dimensionality and W do not affect the width of the shearband. Most notably at small Q, the flow can become very intermittent. This is due to the sudden appearance of load bearing force network configurations [28]. Averaging of the flow field is therefore necessary to obtain the plug flow profile shown in Fig. 1.2b. The flow can also experience complete arrest, due to jamming of the orifice where the particles exit the pipe [29], although this orifice jamming disappears for large enough orifice sizes. Strong dependence of the flow kinematics on particle material stiffness and interparticle friction coefficient was also found [30], although the

average flow profiles obtained in that numerical work are also that of the type indicated in Fig. 1.2b. As for Couette flow, for chute flow, phenomenological equations for the shape of the shearband have been put forward ([25, 28]). The models however all involve exponential shear localization at the edges; usage of such models is based on the assumption that transition state theory ideas can be applied to these flows -- see section 1.5.2.

1.4 Slow Flows in the Split-Bottom Geometry

This thesis will concern itself mostly with granular flows in so-called split-bottom geometries. In this section we will review the results of recent experiments and numerical work on the flows which have been generated in these special flow geometries.

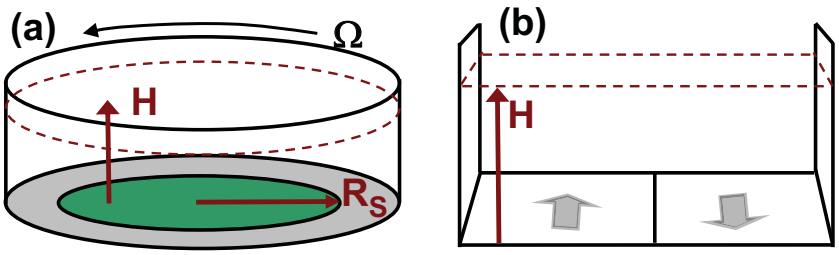

Figure 1.3: (a) Cylindrical split-bottom geometry, showing a disc of radius R_s at the bottom of a granular layer of depth H. Here, the outer cylinder rotates with rate Ω and the bottom disc is kept fixed -- the alternative geometry, with fixed outer cylinder and rotating disc is also frequently encountered. (b) Linear split-bottom geometry, where a container is split along a straight line in its bottom. This geometry can be seen as the $R_s \to \infty$ limit of the cylindrical cell.

1.4.1 General Description

The essential feature of the split-bottom is that it drives the granular medium not directly from the sidewalls, but only from the bottom. The bottom of the container that supports the grains is split in two parts that slide past each other. This way, one takes advantage of gravity to drive the granulate from the sliding discontinuity in the bottom support of the grain layer. This effectively creates and pins a wide shear zone away from the sidewalls. The resulting grain flows

are smooth and robust, with both velocity profiles and the location of the shear zones exhibiting simple, grain independent properties.

In this section, we focus on the rate independent regime. Two variants of the split-bottom geometry will be encountered: in experiments one typically employs a cylindrical split-bottom shear cell, consisting of a bucket, at the bottom of which a disc rotates with respect to the bucket (Fig. 1.3a) [31--34], while for theoretical studies the linear split-bottom cell with periodic boundary conditions is more convenient (Fig. 1.3b) [35--38].

1.4.2 Parameters and Regimes

The cylindrical split-bottom geometry is characterized by three parameters. The radius of the bottom disc R_s and its rotation rate Ω are generally fixed in a set of experiments, and the relative motion of disc with respect to the cylindrical container drives the flow. The thickness of the granular layer, H, is the control parameter that typically is scanned in a series of experiments. Note that the radius of the container appears immaterial, as long as it is sufficiently large (25% larger than R_s appears to be sufficient [32]).

We denote the ratio of the averaged azimuthal velocity of the grains $v_\theta(r)/r$ and the disk rotation speed Ω by ω; $\omega = 0$ thus corresponding to stationary grains, while $\omega = 1$ corresponds to grains comoving with the driving. For the small Ω of interest here (typically less than $0.1\,\mathrm{s}^{-1}$), the flow profiles $\omega(r, z)$ appear independent of Ω -- the flow is rate independent, and transients are short lived. Since centrifugal forces are negligible for typical sizes of R_s (typically a few cm), one may also fix the disc and rotate the bucket, and essentially obtain the same sort of flows with $\tilde{\omega}(r, z) = 1 - \omega(r, z)$ -- see [31--33]. The two remaining parameters, H and R_s, set the large scale structure of the flow.

When the disk rotates, a shear zone propagates from the slip position R_s upwards and inwards. The qualitative flow behavior is governed by the ratio H/R_s, and three regimes can be distinguished. A regime of shallow layers is found for $H/R_s < 0.45$, and here the shear zone reaches the free surface. The three-dimensional shape of the shear zones is roughly that of the cone of a trumpet, with the front of the trumpet buried upside down in the sand. Another regime of deep layers plays a role for $H/R_s > 0.65$, and here the shear zone essentially forms a dome-like structure in the bulk of the material; little or no shear is observed at the free surface. In between there is an intermediate regime, where the shear in the bulk of the material is a mix between the trumpet and dome-like shape.

1.4.3 Surface Flow

Shallow flows -- We first focus on the flow observed at the free surface. For shallow layers, a narrow shear zone develops above the split at R_s, and when H is increased, the shear zone observed at the surface broadens continuously and without any apparent bound. Additionally, with increasing H, the shear zone shifts away from R_s towards the center of the shear cell.

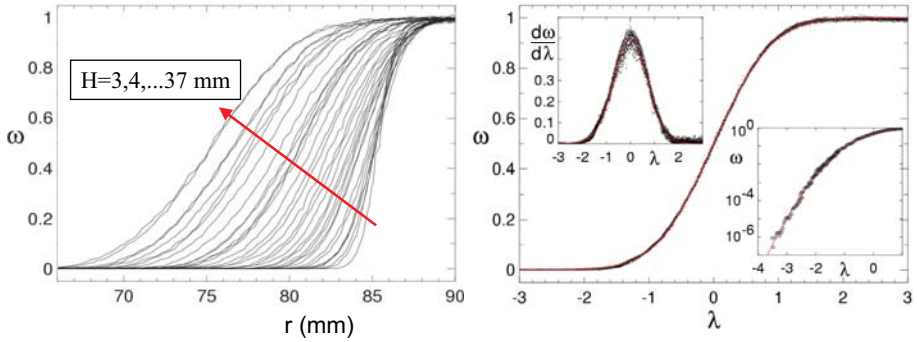

Figure 1.4: (a) Surface flows for glass beads of diameter 300 μm and a range of filling heights H as indicated are well described by an error function (fit not shown) - R_s = 85 mm here, and the outer cylinder is rotating. (b) Collapse of the surface flow profiles shown in (a) and comparison to error function. The rescaled radial coordinate λ is defined as $(r - R_c)/W$. Top inset: strain rates are Gaussian. Bottom inset: the tail of flow profile corresponds well to the Gaussian tail of the error function. Figure reprinted with permission from Ref. [31]. Copyright (2003) by Nature Publishing Group.

After proper rescaling, all bulk profiles collapse on a universal curve which is extremely well fitted by an error function:

$$\omega(r) = \frac{1}{2} + \frac{1}{2} erf\{\frac{r - R_c}{W}\}, \tag{1.3}$$

where *erf* denotes the error function, r is the radial coordinate, R_c the center of the shearband (where $\omega(r) = 0.5$) and W the width of the shearband (Fig. 1.4). Accurate measurement of the tail of the velocity profile further validate Eq. (1.3), and rule out an exponential tail of the velocity profile (Fig. 1.4b). The strain rate is therefore Gaussian, and the shear zones are completely determined by their centers R_c and widths W.

Particle shape does not influence the functional form of the velocity profiles, in contrast to the particle dependence found for wall-localized shear bands in a

Couette cell [16]. For these, the vicinity of the wall induces the formation of semi-crystalline particle layers, in particular for monodisperse mixtures. Apparently such layering effects play no role for these bulk shear zones.

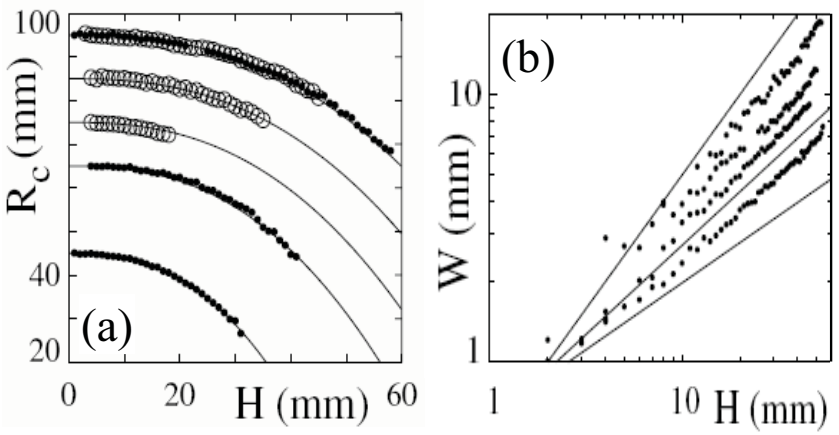

Figure 1.5: (a) Shear zone positions R_c versus H, where R_s = 95, 85, 75, 65, and 45 mm. Lines correspond to Eq. 1.4. (b) Log-log plots of W for spherical glass beads of increasing sizes (ranging from average diameter 300 μm to 2 mm) for R_s = 95 mm. The lines shown in (b) correspond to exponents of 1/2, 2/3, 1. Figure reprinted with permission from [32]. Copyright (2004) by the American Physical Society.

Remarkably, the shear zone center, R_c, turns out to be independent of the material used (Fig. 1.5a). Therefore, the only relevant length-scales for R_c appear to be H and R_s. We find that the dimensionless "displacement" of the shear zone, $(R_s - R_c)/R_s$, is a function of the dimensionless height (H/R_s) only. The simple relation

$$(R_s - R_c)/R_s = (H/R_s)^{5/2} \tag{1.4}$$

fits the data well (Fig. 1.5a).

The relevant length scale for the shear zone width W defined above is given by the grain properties, and is independent of R_s (Fig. 1.5b). Grains shape, size, and type also influence $W(H)$: irregular particles display smaller shear zones than spherical ones of similar diameter. The best available experimental data shows that

$$W/d \sim (H/d)^{2/3}\,, \tag{1.5}$$

where d denotes the particle diameter, although this scaling has not been checked over more than a decade.

The available numerical data coming from molecular dynamics simulations essentially confirm this picture [34, 36, 37, 39]: the surface flows in split-bottom geometries for $H/R_s < 0.45$ are given by Eqs. 1.3-1.5. Only the absolute width of the shear zone remains as a fit parameter, but once this width has been measured for a single value of H/R_s, Eq. 1.5 can be used to estimate the width for the whole range of $H/R_s < 0.45$.

Deep flows: symmetry breaking and precession -- When H/R_s is small, the core material rests on and co-moves with the center disc. With increasing H/R_s, the width of the shear zone grows continuously, and its location moves inward towards the central region (Eq. 1.4). This implies that for deep layers qualitatively different flow patterns can be expected to occur.

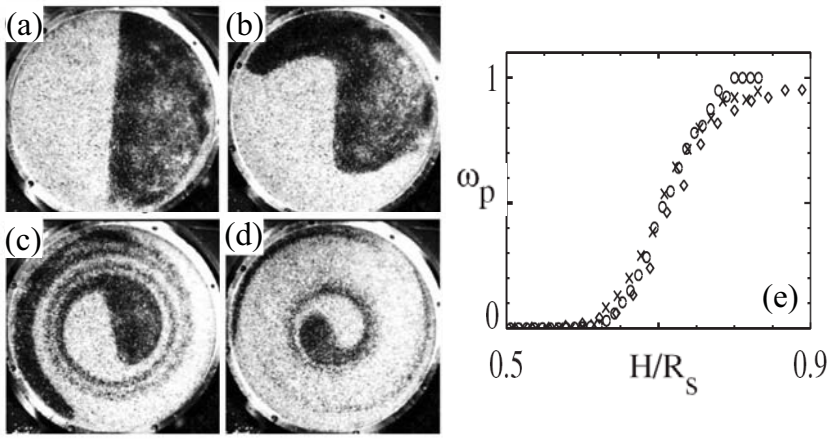

Figure 1.6: Core precession in a split-bottomed geometry. (a-d) Series of snapshots of top views of a setup with stationary disc and rotating outer cylinder (for R_s = 95 mm, H = 60 mm, and rotation rate Ω = 0.024 rps), where colored particles sprinkled on the surface illustrate the core precession for t = 0 s (a), t = 10 s (b), t = 100 s (c) and t = 1000 s (d). (e) Data collapse of the precession rate ω_p for R_s = 45 mm (diamonds), R_s = 65 mm (x) and R_s = 95 mm (circles) when plotted as a function of H/R_s. Figure reprinted with permission from Ref. [33]. Copyright (2006) by the American Physical Society.

The most striking feature of these flows is that the core, as observed at the free surface, now precesses with respect to the bottom disc - hence material in the central part of the system no longer rests on the disc, and there is *torsional failure* of the core. Precession is not simply a consequence of the overlap of

two opposing shear zones, since before being eroded by shear, the inner core rotates as a solid blob for an appreciable time (Fig. 1.6a-d).

The precession rate ω_p is defined as the limit of $\omega(r)$ for r going to zero, where we assume, for simplicity, that the outer bucket rotates with rate Ω and the bottom disc is kept fixed, as in [33] -- consistent results are found in a setup where the disc was rotated and the outer cylinder kept fixed [34]. For various slip radii, the onset height for precession grows with R_s, and the data for ω_p collapses when plotted as a function of H/Rs (Fig. 1.6e). When H/R_s becomes of order one, the whole surface rotates rigidly with the rotating drum and all shear takes place in the bulk of the material. On the other hand, for $H/R_s < 0.65$, hardly any precession can be observed.

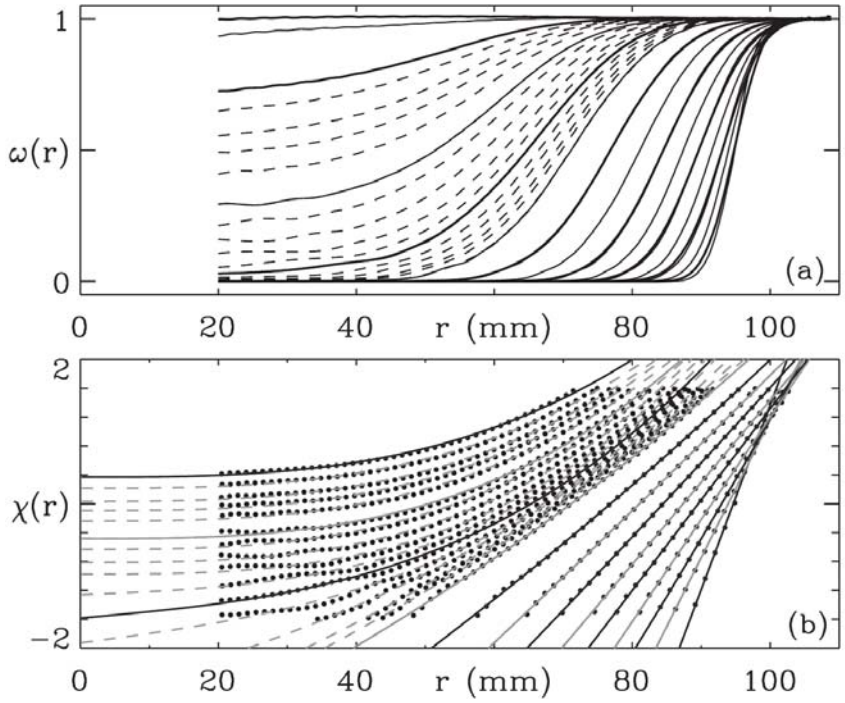

Figure 1.7: Surface velocity profiles $\omega(r)$ for $R_s = 95$ mm and increasing layer depth H. Thick curves: $H = 10, 20 \ldots 80$ mm; Thin curves $H = 15, 25, \ldots 75$ mm; Dashed curves $H = 56, 57, \ldots 69$ mm. (a) Precession gradually sets in for $H > 60$ mm. (b) Corresponding profiles of $\chi(r)$ (dots, see Eq. 1.6), compared to cubic fits given by Eq. 1.7 (curves). Figure adapted from [33].

Intermediate regime and symmetry breaking -- In the intermediate regime, $0.45 < H/R_s < 0.65$, a precursor to the transition to precession can be observed, since a careful analysis reveals that the surface velocity profiles $\omega(r)$ increasingly become asymmetric for $H/r_s > 0.45$. In fact, one can generalize Eq. 1.3 by writing

$$\omega(r) = \frac{1}{2} + \frac{1}{2} erf(\chi(r)) , \tag{1.6}$$

and by fitting the data for $\omega(r)$ over the whole range of H/R_s to this equation (Fig. 5), one finds that $\chi(r)$ can be fitted well by a cubic polynomial of the form

$$\chi(r) = a_0 + a_1 r + a_3 r^3 . \tag{1.7}$$

For shallow layers, $a_3 = 0$, and a_0 and a_1 follow from the scaling laws Eqs. 1.4 and 1.5. For $0.45 < H/R_s < 0.65$, a_3 starts to grow and governs the symmetry breaking of the flow profiles, while for deep layers ($H/R_s > 0.65$), a_1 tends to zero, and a two parameter fit describes the flow profiles well again.

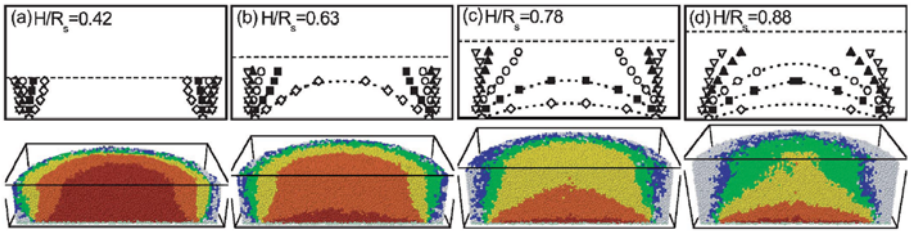

Figure 1.8: Contours of constant angular velocity ω, for different filling height H. Upper panels: MRI experiments: $\omega = 0.84$ (diamonds), 0.24 (squares), 2.4×10^{-2} (circles), 2.4×10^{-3} (triangles), and 2.4×10^{-4} (inversed triangles). Dashed lines indicate H and dotted lines are guides to the eye. Lower panels: simulations. Color is used to identify velocity ranges: dark red, $\omega \in [0.84, 1]$; orange, $\omega \in [0.24, 0.84]$; yellow, $\omega \in [2.4 \times 10^{-2}, 0.24]$; green, $\omega \in [2.4 \times 10^{-3}, 2.4 \times 10^{-2}]$; blue, $\omega \in [2.4 \times 10^{-4}, 2.4 \times 10^{-3}]$; grey, $\omega \in [0, 2.4 \times 10^{-4}]$. Figure reprinted with permission from [34]. Copyright (2006) by the American Physical Society.

1.4.4 Bulk Flow

Shallow flows -- The bulk structure of granular flows is harder to access, but by now, we have information on split-bottom flows from experiments that bury and excavate colored beads [32], MRI [34,40] and numerical simulations [34,36,37,39]. First, for shallow layers, the flow profiles at fixed depth z below the surface H still

takes an error function form, which allows us to characterize $\omega(r)$ at fixed z with the same two parameters R_c and W as before. The location of the shear zones in the bulk where found to be consistent with a scaling argument put forward by Unger *et al.*. The idea is follows: Eq. 1.4 gives the location R_c at the free surface. Then to obtain R_c at depth z, one imagines a systems with a depth of $H - z$, and by inverting Eq. 1.4, obtains where the split would have to be in a system of depth of $H - z$ for the surface location to be as given [41]. This yields:

$$z = H - R_c \left[1 - R_c/R_s(1 - H/R_s)^{2.5})\right]^{1/2.5} . \tag{1.8}$$

The width $W(z)$ of the shear zones is harder to obtain reliably, but the best available experimental data suggest a power law growth of the form $W \sim z^a$, where a is less than 1/2 and more than 1/4 [32, 35]. More recent numerical studies [37] found that $W(z)$ can be well described by a ''quarter circle'' curve of the form

$$W(z) = W(z = H)\sqrt{1 - (1 - z/H)^2} . \tag{1.9}$$

Deep Flows -- The symmetry breaking and the eventual disappearance of grain motion at the surface indicates that qualitatively different bulk flow is developing: the trumpet shape of the shear zones present in shallow layers must have changed. When H/R_s is sufficiently large, the shear zone is entirely confined to the bulk of the material, and forms a dome-like structure above the rotating disk [33, 34, 40, 41] -- see Fig. 1.8. The torsional failure of the material is thus concentrated in the dome. Cheng *et. al.* measured the functional form of the axial velocity profile $\omega(z)|_{r=0}$, and found it to be described by a Gaussian:

$$\omega(z, r = 0) = \omega_p + (1 - \omega_p) \exp -z^2/(2\sigma^2) , \tag{1.10}$$

where ω_p is the rotation rate observed at the surface at $r = 0$, which decreases roughly exponentially with H, and σ, the width of the bulk Gaussian velocity profile, is approximately $R_s/5$ [34].

Couette versus split-bottom geometries -- The first studies [31] of split-bottom geometries where done in a modified Couette cell, as shown in Fig. 1.9. The resulting flows are similar to the disc geometry, as long as the shear flow is away from the side walls, but since for increasing filling heights the shear zones move inward, they will inevitably ''collide'' with the inner cylinder for sufficiently large filling height. The resulting flow profiles are shown in Fig. 1.9 [42].

First, one observes that for sufficiently large H, the flow profiles become independent of H. The main result is that the tail of these flow profiles becomes purely exponential for large H, while it is Gaussian for shallow H. We have found

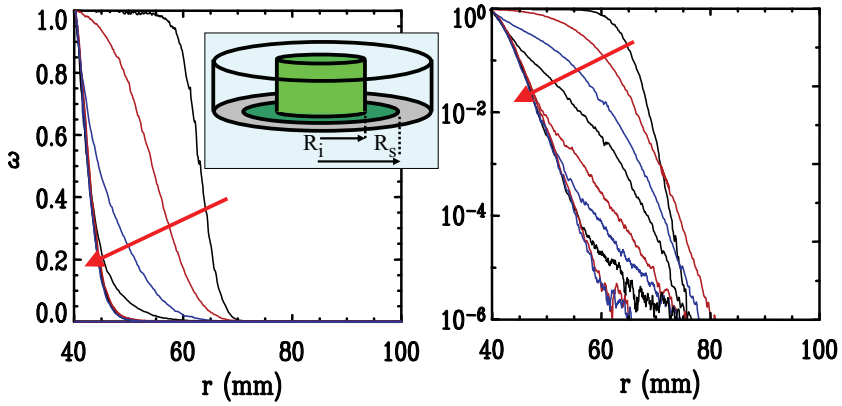

Figure 1.9: Surface flow profiles observed for 1 mm glass beads in a split-bottom Couette geometry, with inner cylinder radius R_i = 40 mm, a split at R_s = 65 mm, and H = 10, 30, 40, 50, 60, 70, 80, 100, 110 mm. The outer cylinder is 120 mm. Figure from Ref. [42].

this exponential talk to be robust, i.e., independent of grain shape. Note that this does not contradict the findings of Mueth *et al.* -- these concern the shape of the flow profile near the shearing wall, corresponding to the range $10^{-3} < \omega < 1$ -- flow profiles are indeed grain dependent here. But further out in the tail they become purely exponential. For other examples of exponential tails see [43].

1.4.5 Dilatancy

By means of Magnetic Resonance Imaging, direct measurements of the evolution of the local packing density of the shear flow generated in a cylindrical split-bottomed geometry were performed in [40]. To be able to image the particles by means of MRI, food grade poppy seeds were used; these contain MRI-detectable mineral oils.

It was observed that the relative change in density in the flowing zone is rather strong and saturates around 10-15 % -- likely the rough and peanut shape of the poppy seeds plays a role. After long times, a large zone with more or less constant, low packing fraction forms, encompassing most of the shearband. The fact that the density remains constant here, even though local strain rates vary over many decades, suggests that the density of the flowing material is a function of the *total strain*, and not of the strain rate, similarly to what was

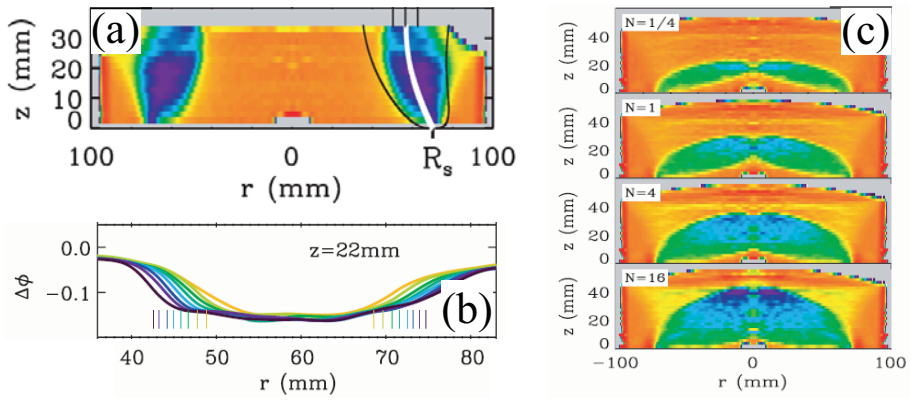

Figure 1.10: Evolution of dilatancy. (a) Color map of relative density change (light blue corresponds to -10%) for $H/R_s = 0.51$ after 4 rotations of the bottom disk (b) Spread of dilated zone for vertical shear observed in the bulk at $H/R_s = 0.51$ at $z = 22$ mm ($H = 36$ mm), for $N = 1/2, 1, 2, \ldots, 64$, compared to estimates where, after N turns, the local strain equals one. (c) Spread of dilatancy for dome-like flow observed at $H/R_s = 0.77$, for number of disc rotations N as indicated. Figure reprinted with permission from Ref. [40]. Copyright (2008) by EDP Sciences.

observed by Kabla [15].

Consistent with this, the dilated zone was found to slowly spread throughout the system as time progresses (Fig. 1.10). This spread is consistent with the idea that, after initial preparation, the accumulated local strain governs the amount of dilatancy -- to show this, the flow field in the bulk was reconstructed by combining the above mentioned scaling relations for the location and width of the shear zones in the bulk, and this reconstructed flow field can then be compared to the density field obtained by MRI. Such comparison shows that the locations of the dilated zone and the shear zone coincide, for small filling heights ($H/R_s < 0.6$). Finally, for deep filling heights where torsional failure and precession play a role, a relatively long-lived transient was found to cause the dilated zone to deviate substantially from the late-time shear zone.

1.5 Theory for Granular Flows

Our focus is on slow flows, for which over the years a variety of theories have been put forward. These theories have been successful by varying degree, but as yet, no theory can capture all the physics of slow granular flows. It

remains for example remarkable that no theoretical framework is available from which Eqs. 1.3-1.5 can be deduced. Creating such a theory would constitute an important milestone in the development of our understanding of slow granular flows.

Much progress has however been made in the study of the 'liquid'-like granular flows, with the development of the so-called Inertial number theory. So although applied only to faster flows, that theory serves as a good starting point of the discussion of slow granular flow theories, the subject of this section. After the treatment of the fast flow theory, we will give an overview of essential characteristics that slow granular flow theories should at least capture. Then we will discuss the theoretical framework used in the analysis of the split-bottom flows. We choose to treat this geometry here, since it is the geometry we will be using in our experimental exploration of slow granular flows in the rest of this thesis.

1.5.1 Fast Flows

In describing fast dry granular flows, such as steady granular flows down an incline, much progress has been made in recent years. For a comprehensive review, see Ref. [2]; in this section we will give a brief overview of the main results. In fast granular flows, large flowing zones are observed, and simple, steady state fluid properties emerge. Microscopically, momentum exchange in these fluid-like flows takes place by a mixture of collisions, as in the granular gas, and enduring frictional contacts.

The inertial number -- It turns out that the only simple dimensionless parameter one can construct with the variables playing a role in these flows, is the inertial number[1]: the local pressure P, the strain rate $\dot{\gamma}$, the particle diameter d and the particle density ρ can be combined to give:

$$I = \frac{\dot{\gamma} d}{\sqrt{P/\rho}}. \tag{1.11}$$

This number characterizes the local 'rapidity' of the flow. One particularly elegant interpretation views it as the ratio of two timescales in granular flows: $\dot{\gamma}$ is a timescale set by the flow rate, and $d/\sqrt{P/\rho}$ is the timescale a particle needs to travel over its own diameter in free space, given that it is subjected to a force Pd^2 -- it is the timescale at which granular rearrangements take place in a semi-dilute granular flow, where the weight that exerts a pressure P on a

[1] Assuming the particle are hard, otherwise particle elasticity becomes relevant [44].

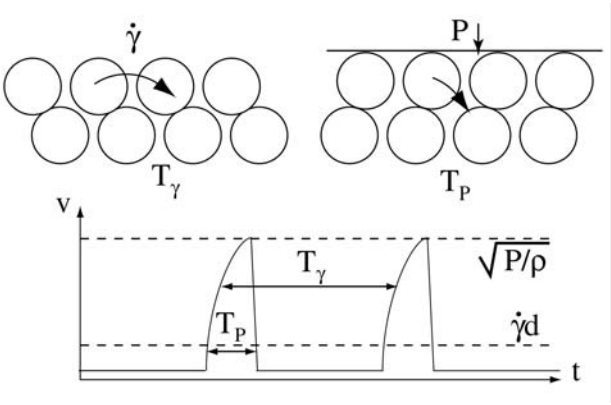

Figure 1.11: The rearrangement process of a particle inside a granular flow. $T_{\dot{\gamma}}$ is the rearrangement timescale, T_P is the confinement timescale. Figure reprinted with permission from Ref. [12]. Copyright (2004) by EDP Sciences.

particle is sometimes not balanced by the presence of another particle, which also implies or requires that there is space for particles to move around. See Fig. 1.11.

Shear stress -- The local stress in these flows is proportional to the local pressure. Assuming that the local dissipation is still predominantly frictional, one writes for the local stress τ:

$$\tau = \mu(I)P, \tag{1.12}$$

with $\mu(I)$ an effective friction coefficient that depends on the inertial number. $\mu(I)$ is an empirical function of I, and involves material parameters:

$$\mu(I) = \mu_s + \frac{\mu_2 - \mu_s}{I_0/I + 1}. \tag{1.13}$$

The friction coefficient μ starts at μ_2 in the limit of very small strain rates, where only frictional interactions play a role. Note that μ_2 is an effective friction coefficient, not necessarily equal to the interparticle friction coefficient μ_p. $\mu(I)$ increases around I_0 to its maximum value μ_s. Typical values of I_0 are around 1.

This local relation between stresses, strain-rates and I then successfully captures many aspects of these rapid granular flows [12], and can even be generalized to three-dimensional flows [2, 45].

The three-dimensional generalization gives a good intuition for the type of flow behavior that the inertial number theory predicts at small strain rates. The

stress tensor in three dimensions is given in the following form:

$$\sigma_{ij} = P\delta_{ij} + \tau_{ij}, \tau_{ij} = \eta(|\dot{\gamma}|, P)\dot{\gamma}_{ij}, \tag{1.14}$$

with δ_{ij} the Kronecker delta and $\dot{\gamma}_{ij} = \partial u_i/\partial x_j + \partial u_j/\partial x_i$ the full strain rate tensor; u_j is the velocity component in direction j. The viscosity η in this framework varies throughout the material in the following way:

$$\eta(|\dot{\gamma}|, P) = \mu(I)P/|\dot{\gamma}|. \tag{1.15}$$

The notable feature in this equation is the dependence of the viscosity on the modulus of the strain rate $|\dot{\gamma}|$ -- in the limit of slow flows, the viscosity diverges. This feature lets the inertial number theory capture the property that granular materials have a yield stress $\tau_Y = \mu_s P$; only if $\tau > \mu_s P$, flow is possible.

Dilatancy -- The local volume fraction Φ of a flowing zone depends on the inertial number , and typically decreases from Random Close Packing [46] at small I to values around 0.7 [23] in two dimensions and as low as 0.55 [2] in three dimensions at large I.

Taking dilatancy into account in modeling of granular flows is not always necessary: in the three dimensional generalization of the inertial number-based model, good quantitative agreement between numerics and experimental results were obtained [45] even though the small density variations throughout the shearing layer were neglected. However, dilatancy effects can be used to capture transients in granular flows, for example for submersed flows [47], and they are also used to describe an instability in inclined plane flows [48].

1.5.2 Slow Flows -- General Considerations

Soil mechanics is a natural starting point to describe rate independent flows, since in this limit, the microscopics are dominated by enduring frictional contacts. Both rate independence and the emergence of (narrow) shear bands are consistent with a Mohr-Coulomb picture where the friction laws acting at the grain scale are translated to the stresses acting at coarse-grained level. The idea is that when ratio of shear to normal stresses is below the yielding threshold, grains remain quiescent, while in slowly flowing regions the shear stresses will be given by a (lower) dynamical shear stress.

This way of thinking readily captures the maximal slope of dry sand piles. However, the steep gradients associated with narrow shear bands are difficult to capture by a continuum theory, and shear bands often are described as having

zero width [41]. Another difficulty for continuum models is that the width of the shearbands usually depends simply on the grain scale, and is therefore thought to disappear in the continuum limit [49], where one takes $d \to 0$.

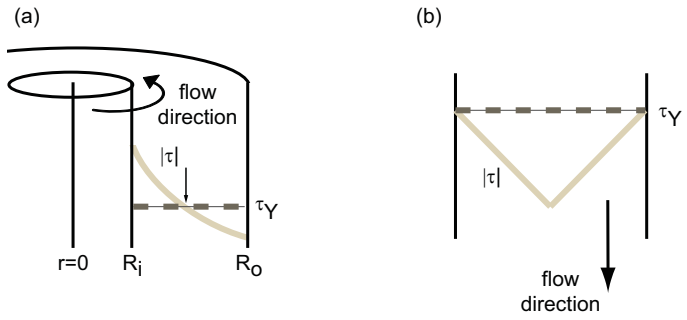

Figure 1.12: The stress field in two flow geometries. (a) Couette; (b) chute flow. Light grey indicate the locally applied stress, the dark grey dashed line indicates where the macroscopic yield stress is. At the arrow, the local stress drops below the yield stress.

Constitutive equations -- For the rate independent regime, obviously constitutive relations based on relating stresses and strain rates are unlikely to capture the physics, as they do so successfully in the inertial regime.

This was for example shown in Ref. [23]. There they obtained numerically the local strain rates in a Couette geometry. For steady Couette flow, continuum mechanics gives the form of the stress component $\sigma_{r\theta}$ distribution in the gap:

$$\sigma_{r\theta}(r) = \sigma_{r\theta}(R_i)(\frac{R_i}{r})^2, \tag{1.16}$$

from conservation of torque. $\sigma_{r\theta}(R_i)$ is the stress exerted by the inner wheel. This stress profile is shown in Fig. 1.12a. In the Couette geometry, the local strain rates can then be compared to the local stress, to see if any constitutive equation $\tau(\dot{\gamma})$ can be found. For slow driving, it was found that this is not possible [23]. Interestingly, for moderate to fast driving, a Bingham relation between the local stress and strain rates

$$\mu(I) = \mu_{min} + bI, \tag{1.17}$$

with b a constant was obtained. This is expected based on the behavior of $\mu(I)$ for low to intermediate I -- see Eq. 1.13 and Fig. 10 in Ref. [23].

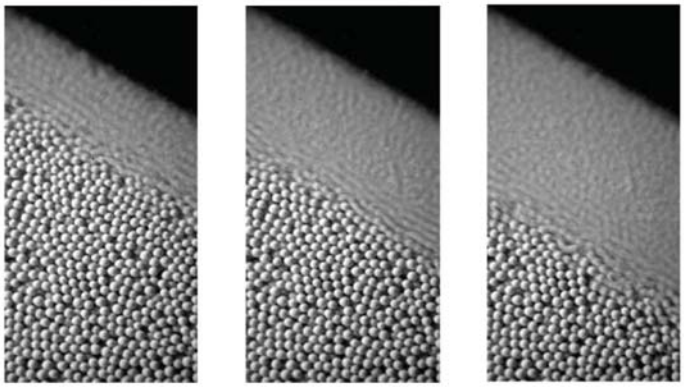

Figure 1.13: Creeping flow deep into a heap, onto which beads are continuously poured onto. After hours of flow at the surface, motion of the particles is observed even deep into the pile. Figure reprinted with permission from Ref. [50]. Copyright (2001) by the American Physical Society.

Yield stress -- Another profound problem in slow granular flows is that locally, flow can occur, even though the local stress has dropped below the global yield stress. This is evident in heap flow experiments, where even deep into the pile purely exponential flow profiles are observed, as was shown convincingly by Komatsu [50] (see Fig. 1.13), and experimentally confirmed over 6 orders of magnitude in flow rate in Ref. [43] by means of both Particle Image Velocimetry (PIV) and light scattering methods. The exponential profiles suggest that the flow goes smoothly to zero at the boundary of the flow geometry, instead of abruptly at the yield stress.

The role of fluctuations -- The failure of local rheologies for slow flows has stimulated the formulation of several non-local rheologies. A Kramer-Eyring transition state theory of activation rate process was invoked [28] in chute flows. This is a reasonable first guess, due to the particular form of the stress profile in the chute flow geometry. This stress profile is shown in Fig. 1.12b. Close to the wall, the stress τ on the granular flow is close to the yield stress of the material, which leads to zero shear velocity at the walls. Small fluctuations in the stresses close to the wall could then cause the material to intermittently experience stresses above the yield stress there, allowing local flow near the boundary. This physical picture was used to explain the exponentially localized shearbands, although the experimental resolution was not good enough to test the model

in great detail.

Other models invoking granular fluctuations were also proposed, for example a granular temperature in Ref. [20] to explain the shape of velocity profiles observed in Couette flows, or randomly varying local material failure strength [38, 51] to explain the finite width of the shearbands in the split-bottom geometry. Bazant put forward his 'spot'-model, which is based on the assumption that slow, dense granular flows are best described with a diffusion of low density regions in the material, called *spots* [52]. The two-dimensional model describes flow profiles in chute flow and Couette geometries reasonably well. However, recently it was shown [53] that the very structure of this model is incapable of capturing the observed velocity profiles in the split-bottom geometry.

1.5.3 Slow Flows -- Split-Bottom

The flows in split-bottom geometries have been simulated both by molecular dynamics simulations [34, 36, 39] as well as by contact dynamics [37], and a wide number of theoretical approaches have been put forward, including the spot model [54] and various other stochastic flow models [38, 51]. We briefly discuss some of these approaches here.

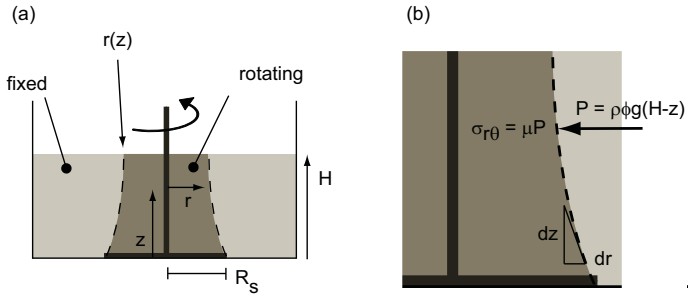

Figure 1.14: (a) An arbitrary shear zone of zero width $r(z)$ separates a rotating inner core and a static outer body. In (b): The frictional stress $\sigma_{r\theta} = \mu P$ on the shearing surface can be integrated to give the total driving torque necessary to rotate the disk in red. The integral is given in Eq. 1.18.

Variational principle -- The first attempt to describe the flows in split-bottomed geometries goes back to Unger and coworkers [41]. The flows are treated in a Mohr-Coulomb fashion, with shear bands of zero width. The idea is

to minimize the energy dissipation needed to sustain the flow. Calculating the total friction along the shear-sheet $r(z)$ using assumptions of constant friction coefficient μ and hydrostatic pressure P, amounts to finding the minimum of the functional

$$T(H) = 2g\pi\rho\Phi\mu \int_0^H (H-z)r^2\sqrt{1+(dr/dz)^2}dz \tag{1.18}$$

Here ρ is the bulk density of the particles, Φ is the average packing fraction ($\sim$ 0.59 [2]) and μ is the effective friction coefficient. Identifying $r(z)$ with the center of the shearband $R_c(z)$, minimizing Eq. 1.18 gives predictions for the location of the shearbands in the split-bottom geometry. The location of the shear zones predicted for shallow layers are very close to those observed, and for deep layers the model predicts a hysteretic transition to dome-like shear. Hence, while a number of aspects of split-bottom flows can be captured already by this simple model, the hysteretic transition and zero width of the shear bands are clearly in contrast to experimental findings.

In subsequent work [51], this minimal dissipation model was extended by combining the variational principle with a self organized random potential as follows. At any given time, the shear band is still represented as having zero width. However, the granular material is now taken to be inhomogeneous, with a local strength field which varies with space and is updated every timestep. At any given time the surface that minimizes the torque can be obtained, after which the strength field is updated etc. A smooth flow profile is then obtained by averaging over the different shear bands. The resulting flow fields are very close to those observed experimentally, with the only adjustable parameter controlling the effect of disorder. One possible point of criticism is that the model assumes that the fluctuating shear bands are radially symmetric (see [38] for details).

Inertial flows -- Jop performed simulations of flows in a cylindrical split-bottom setup [55], using the 'inertial number' theory described in section 1.5.1. The location of the shear zones in the bulk, the smooth transition to precession and the dome flows were all recovered. The width of the shear zones was found to scale with driving rate as $\Omega^{0.38}$, and indeed for slow flows the shear zones attain zero width. The inertial model therefore does not fully capture the physics of the slow split-bottom flows, but it does slightly better than Ungers original model [41] in that it captures the smooth transition to precession.